Superconductor Science and Technology

Mechanical design of a superconducting demonstrator for magnetic density separation

To cite this article: J J Kosse *et al* 2021 *Supercond. Sci. Technol.* **34** 115019

OPEN ACCESS
IOP Publishing
Superconductor Science and Technology
Supercond. Sci. Technol. **34** (2021) 115019 (17pp)
https://doi.org/10.1088/1361-6668/ac2c0f

Mechanical design of a superconducting demonstrator for magnetic density separation

J J Kosse, W A J Wessel, C Zhou, M Dhallé, G Tomás, H J G Krooshoop, H J M ter Brake and H H J ten Kate

The University of Twente, Netherlands

E-mail: j.j.kosse@utwente.nl

Received 8 July 2021, revised 16 September 2021
Accepted for publication 1 October 2021
Published 14 October 2021

Abstract

The focus of this paper is on the mechanical design of a NbTi-based demonstrator magnet for *magnetic density separation* (MDS) that is being constructed at the University of Twente. MDS is a new recycling technology that allows the separation of non-magnetic particles based on their mass density, using a vertical magnetic field gradient and a ferrofluid. The unique mechanical design challenge for this type of magnet is the desired minimization of the distance between a ~1 m^2 planar array of cryogenic racetrack coils and the ambient-temperature ferrofluid bath. The optimization of the magnet geometry results in a distance between the coils and ferrofluid of 50 mm. This is made possible by opting for conduction-cooling, for the inclusion of room-temperature rods that pass through the cold mass to support the cryostat, and for the geometry of the cassette that reacts to the Lorentz force.

Keywords: vertical magnetic field gradient, racetrack, magnet, magnetic density separation, ferrofluid, superconductor, mechanical

1. Introduction

At the University of Twente a superconducting NbTi demonstrator magnet for *magnetic density separation* (MDS) is under construction. MDS is a new recycling technology that allows to separate non-magnetic materials based on their mass density [1–6] and that ideally requires a magnetic field with a magnitude that only changes in the vertical direction. Such a one-directional magnetic field gradient requires a dedicated electromagnet design, as discussed in [12, 14].

In the MDS process, illustrated in figure 1, shredded feed particles are immersed in a superparamagnetic fluid (*ferrofluid*), which flows over a magnet. The fluid, consisting of a carrier liquid (usually water) with a concentration of superparamagnetic nanoparticles dispersed in it [7], is magnetized to saturation by a magnet that generates a vertical magnetic field gradient [1]. Since the fluid is attracted to the magnet but the feed particles are not, the net force on the particles pushes them to an equilibrium height that depends on their mass density. Different-density particles float at different heights in the fluid bed. The horizontal component of the force on the ferrofluid pushes feed particles towards separator blades that collect the different-density streams. After this, the ferrofluid is recovered and the separated feed products go through a sensor sorting process for final purification [6]. A transport belt moves over the magnet to carry away any magnetic particles that might be present in the feed stream.

Compared to alternatives, the MDS process is cost- and energy efficient, potentially providing a significant step forward towards a circular use of resources [2, 5]. The major advantage compared to other types of magnetic separation using a ferrofluid is the ability to separate multiple density fractions in a single process step, whereas the other types of separation are based on a binary sink-float approach [8]. The binary sink-float approach is used for the separation of for example gold [9], diamonds [10] and coal [11].

1361-6668/21/115019+17$33.00

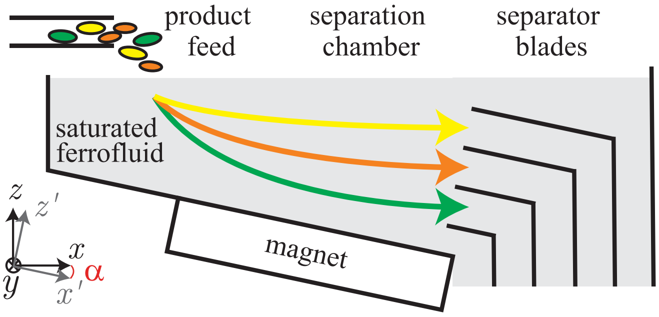

Figure 1. Schematic of an MDS system. Non-magnetic feed particles are immersed in a ferrofluid that is attracted to a magnet. When the magnet is tilted at an angle α with respect to the horizontal, the combination of vertical forces on the feed particles (gravity, buoyancy and effective repulsion by the magnet) dictates their equilibrium height, whereas the horizontal component of the magnetic repulsion pushes them towards the separator blades. An angle α of 12° is used in the demonstrator system [14]. Also indicated are the coordinate systems used in this paper: z is the vertical direction while z' indicates the normal distance to the magnet surface.

The demonstrator magnet will be the first superconducting MDS system. The advantages of superconducting electromagnets compared to the permanent magnets currently used in this technology are discussed elsewhere [12]. A comparison of the performance obtainable for MDS with various technical superconductors is made in [13].

For the derivation of the required coil shape (racetracks), size (length 1.4 m, width 0.3 m, thickness 50 mm per coil) and number (3) of coils for the demonstrator, the reader is referred to [14]. The thermal- and electrical aspects of the design are described in [15], detailing how the coils are cooled to an operation temperature of 4.5 K resulting in a 2 K margin with the current sharing temperature (6.5 K at 5.2 T, 300 A). The present work discusses the design of the magnet to function from a mechanical point of view. It focuses on two main questions:

(a) How to handle the Lorentz force and the attraction force between coils and ferrofluid. This attraction force is estimated to be up to 34 kN for this particular system, designed for the separation of shredded electronic material;
(b) How to minimize the coil-to-fluid distance so that the magnetic field is utilized to its fullest extent. The large planar surfaces that are formed by the bottom of the ferrofluid bed and the top surface of the coils present a unique minimization challenge that is absent in most other applications of superconducting magnets.

Perhaps the closest similar applications of superconducting magnets are wiggler- and undulator magnets for accelerators [16]. Here an horizontal array of racetrack coils is also often used [17]. The main differences are that the undulator coils have a much shorter length compared to MDS, since the volume of interest is just the beam-pipe of the accelerator. Thus, more design freedom is possible for the support structure.

The layout of this paper is as follows: firstly, the cryostat is introduced in section 2. Of course, the main function of the cryostat is to minimize heat transfer towards the coils [18]. To eliminate convection, the vessel is pumped vacuum. From a mechanical viewpoint, this implies that the outer vessel needs to be strong enough to withstand the outside atmospheric pressure as well as the force that pulls the ferrofluid towards the magnet.

Secondly, the mechanical properties of the coils are discussed in section 3. Each coil consists of a winding pack, a mandrel, spacers, side-plates and end-pieces. The winding packs are anisotropic composite materials for which the mechanical properties are derived. The shape of the winding packs are introduced in [14].

Thirdly, the mechanical behaviour of the cold mass is considered in section 4. Besides the coils, this includes their enclosure. This *cassette* consists of two high-strength aluminium alloy machined plates, that enclose the winding packs and are bolted together. During cool-down, they shrink-fit around the coils providing pre-compression. During excitation of the magnet they react to the Lorentz force. Underneath the bottom aluminium alloy plate, several high-purity aluminium heat drains are attached to provide a high thermal conductivity link between coils and cryocooler. Thus the required mechanical- and thermal functions of the cold mass are spatially decoupled.

Finally, the support structure that keeps the cold mass in place in the cryostat is considered in section 5. This structure, made from G11, is optimized to minimize the conductive heat load to the cold mass and to the radiation shield, while providing adequate mechanical strength. Depending on the loading situation, parts of the structure can be under compression or under tension.

Figure 2 gives an idea of how the main system components are arranged in practice. The magnet is tilted 12° relative to the horizontal plane to propel the feed stream [14]. To account for this, two coordinate systems (x, y, z) and (x', y, z') are used throughout the paper: z is the vertical direction, z' is directed normal to the coil surface, x and y are the horizontal components whereas x' is the parallel-to-the-coil direction and lies in the xz-plane with an angle of 12° with respect to x. The feed particles move through the fluid bed in the x-direction, as indicated in figure 1.

Table 1 presents the thickness of the components that separate the coils and the ferrofluid by 50.5 mm.

2. Cryostat

In this section the design of the cryostat is introduced. The cryostat has a main chamber in the shape of a half-cylinder with a flat cover plate (or D-shaped) and is illustrated in figure 3.

The main vacuum vessel has a 20 mm thick flat plate and a 8 mm thick curved section. Attached to this half-cylinder is a turret housing a cryocooler, instrumentation, current leads and other services. This separate turret allows the cooler to work in the optimum orientation and outside the strong magnetic field

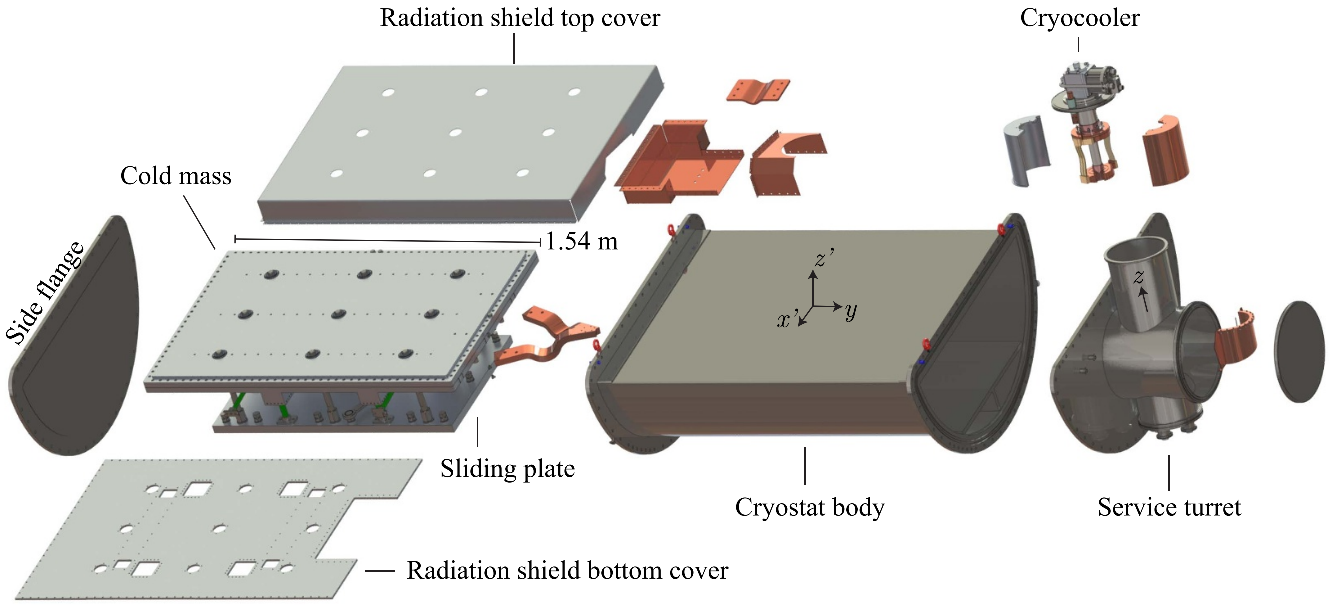

Figure 2. Exploded view of main components of the magnet system. The $x'z'$-plane is rotated 12° clockwise to the xz-plane, z is opposite gravity.

Table 1. Components determining the coil-to-ferrofluid distance, in order of closeness to ferrofluid. The MLI blankets have 10 layers each and take up 3 mm per blanket when uncompressed [19].

Component	Layer thickness (mm)
Cryostat top plate	20
3 MLI blankets and vacuum	12
Radiation shield	2
1 MLI blanket and vacuum	4
Cassette	12
G11 plate	0.5
Total	50.5

region, in this design below 100 mT [20]. The main chamber is made of AISI 304 stainless steel. The magnetic attraction of the plate towards the coils is estimated to be roughly:

$$F_{\mathrm{mag}} = \chi V B \nabla B / \mu_0 \tag{1}$$

$$= 2.7 \cdot 10^{-3} \cdot 0.02 \cdot 2.5 \cdot 25/(4\pi 10^{-7})\ \mathrm{N}\ = 2.7\ \mathrm{kN}. \tag{2}$$

Here the magnetic susceptibility χ of 2.7×10^{-3} is representative for SS304 [18]. V is the volume of the top plate and B the average magnetic flux density. The value 2.7 kN is relatively small compared to the 1 atm ambient pressure (i.e. 160 kN).

The initial concept of the MDS demonstrator assumed a helium bath-cooled NbTi magnet. However, this would require a double-walled cryostat. It was later realized that the flat top plate(s) of the cryostat would need a significant thickness to resist the combination of the outside pressure and the magnetic force from the ferrofluid-magnet interaction. To maximize the vertical gradient of the magnetic field magnitude at the fluid bed, the demonstrator magnet design was optimized to minimize the distance between the coils and the ferrofluid.

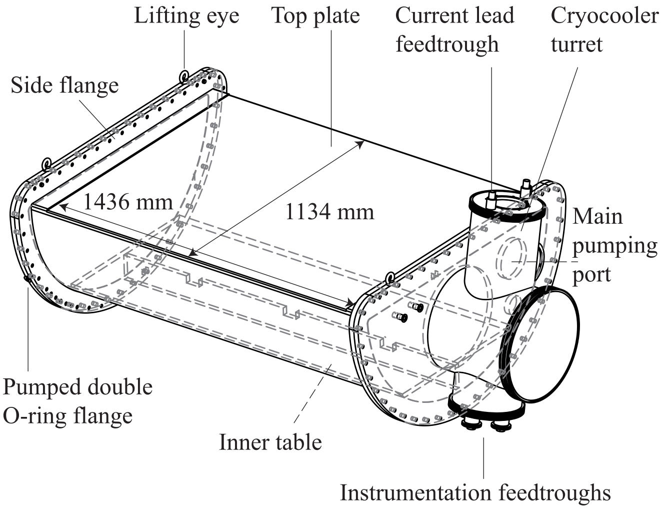

Figure 3. Schematic of the AISI 304 stainless steel MDS cryostat indicating the main vacuum vessel with D-shaped side flanges. The flanges are attached to the main chamber via double O-ring connections. One of the flanges has a turret attached to it which houses the cryocooler and instrumentation ports. The turret is directed vertical whereas the top plate is placed at a 12° angle relative to the horizontal plane. The reason for this tilt is discussed in [14]. Also present in the turret are the current leads. Electrical- and thermal connections are made by accessing the turret via a side-flange with diameter 400 mm. Inside the cryostat a steel table is welded parallel to the top plate. During assembly the cold mass is installed on an aluminium plate, which is then slid onto the steel table. The support structure between cryostat and the floor is not shown.

Thus, it was decided to use a conduction-cooled magnet. Besides the enhanced performance, i.e. a higher vertical magnetic gradient, this also saves material, and reduces in system mass. Also, the absence of cryogens reduces the risk of injury, which is an important feature for use in an industrial environment.

The magnet's cold mass is supported in the main chamber by means of a structure consisting of fibreglass pillars, as further detailed in section 5. The cold mass rests via these pillars on a 40 mm thick aluminium plate which can be slid onto a base table located inside the main chamber. This plate has multiple bolts that assure the parallel positioning of the coils with respect to the top plate, by adjustment of the tip, tilt and distance of the cold mass relative to the plate.

To help minimize the required top-plate thickness, nine stainless steel columns are installed to support the flat top plate, thus minimizing its deflection. The columns pass through holes in the cold mass and stay at room temperature. A single-walled system supported with columns allows an increase in the vertical magnetic field gradient in the ferrofluid of a factor 2 compared to a double-walled cryostat without the column structure.

To verify that the displacements and stresses are acceptable, a FEM analysis was performed of the main chamber. The Young's modulus was set to 198 MPa and Poisson's ratio to 0.2895 [18]. The simulation geometry is illustrated in figure 4(a). The side flanges of the chamber were considered rigid and fixed in this analysis. The applied loads are 1 bar on the outside surfaces, and an extra 0.3 bar on the top plate due to fluid-to-magnet attraction, and the reaction force ($3 \cdot 10^4\ \mathrm{Pa} \times 1.1\ \mathrm{m}^2 = 34\ \mathrm{kN}$) on the aluminium plate where the G11 pillars are mounted. The result, shown in figures 4(b)–(d), indicates that the maximum stress remains below 100 MPa, less than half of the 240 MPa yield strength of SS304 at room temperature [18]. The maximum stress is located at the welds between the top plate and half-cylinder. The maximum deflections of both the half-cylinder and of the top plate are around 0.6 mm. If the stainless steel column structure is omitted in the simulation, the maximum stress increases to 150 MPa and the deflection of the top plate becomes an unacceptable 5.7 mm.

The obtained results for the cryostat without the column structure are compared to analytical results. Consider a clamped rectangular plate with sides a and b undergoing a uniform pressure p. The deflection dz of the centre of the plate is then given by:

$$dz = \frac{12Xpb^4}{Ed^3}\left(1-\nu\right), \tag{3}$$

where X is a scalar depending on the ratio b/a, E is Young's modulus, d is the thickness of the plate and ν Poisson's ratio [22]. Here b is 1.426 m and a is 1.134 m, while p is set to 1.3 bar. For this ratio of b/a, X is around 0.0018. This yields a dz of 5.5 mm, very close to the 5.7 mm found with the FEM simulation.

3. Winding pack composite properties

This section describes the mechanical properties of the winding pack, needed for the simulation of the mechanical behaviour of the cold mass during cool-down and energizing. As discussed in [13], the winding pack of the coils consists of wires containing NbTi filaments, a copper matrix and electrical insulation (Formvar), embedded in epoxy resin (Stycast 2850FT blue). All these materials have different Young's moduli, yield stress and thermal expansion coefficients.

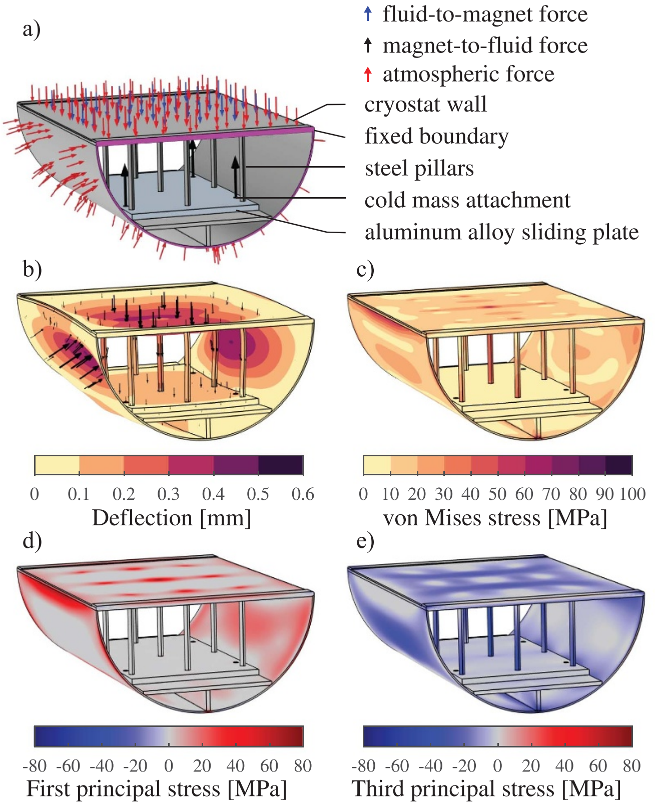

Figure 4. (a) Schematic of the FEM analysis, indicating the main stainless steel chamber, steel support columns and the aluminium alloy inner plate. The arrows give an impression of the forces acting on the cryostat. (b) The deflection of cryostat chamber when subjected to atmospheric pressure and magnet-fluid force. The direction of the deflection is indicated with black arrows. The top plate and sidewall both move up to 0.6 mm inwards. (c) The maximum von Mises stress occurs at the inner (continuous) and outer (disconnected) welds between the top plate and half-cylinder, and is lower than 100 MPa. For the outer weld the stress is mostly tensile, as indicated by the principal stress plot in (d). Compressive regions can be identified in (e), such as the inner welds and the stainless steel pillars.

Since it is not feasible to perform mechanical 3D calculations in which every NbTi strand is explicitly modelled, mechanical properties representing the winding pack as a homogenous material are sought. For simplicity we attribute to the insulation layer the same properties as Stycast, resulting in a three-component composite. The assumption is made that the wire occupies 75% of the winding pack, an estimate that was confirmed during the winding of the coils.

Early on in the design phase, it was foreseen to use a rectangular conductor to wind the racetrack coils, since a higher packing factor is achievable and thus a better performance can be obtained [26]. The conductor was changed to a round cross-section one because it was feared that the rectangular conductor would twist during the coil winding.

Table 2. Mechanical properties at 4.2 K of materials in the winding pack.

Material	Volume fraction	Young's modulus E (GPa)	Poisson's ratio ν	Thermal expansion $293 \rightarrow 4$ K (%)
Copper	0.388	124 [27]	0.345 [28]	−0.324 [18]
NbTi	0.287	82 [27]	0.33 [28]	−0.188 [18]
Stycast 2850FT	0.25	24 [25]	0.3 [31]	−0.53 [32]
Formvar	0.075			

The NbTi/Cu conductor is capable of handling load in the longitudinal direction (indicated as (1) below) better than in the radial directions (2) and (3), which must be transferred via the Stycast. Thus the winding pack has anisotropic mechanical properties. Literature data on impregnated winding packs show that an orthotropic stress–strain relationship gives an accurate description of the behaviour of these composites [29, 30].

The stress–strain relation of an orthotropic material can be written as:

$$\begin{bmatrix} \varepsilon_{11} \\ \varepsilon_{22} \\ \varepsilon_{33} \\ \varepsilon_{23} \\ \varepsilon_{31} \\ \varepsilon_{12} \end{bmatrix} = \begin{bmatrix} \frac{1}{E_1} & -\frac{\nu_{21}}{E_2} & -\frac{\nu_{31}}{E_3} & 0 & 0 & 0 \\ -\frac{\nu_{21}}{E_2} & \frac{1}{E_2} & -\frac{\nu_{32}}{E_3} & 0 & 0 & 0 \\ -\frac{\nu_{31}}{E_3} & -\frac{\nu_{32}}{E_3} & \frac{1}{E_3} & 0 & 0 & 0 \\ 0 & 0 & 0 & \frac{1}{2G_{23}} & 0 & 0 \\ 0 & 0 & 0 & 0 & \frac{1}{2G_{31}} & 0 \\ 0 & 0 & 0 & 0 & 0 & \frac{1}{2G_{12}} \end{bmatrix} \begin{bmatrix} \sigma_{11} \\ \sigma_{22} \\ \sigma_{33} \\ \sigma_{23} \\ \sigma_{31} \\ \sigma_{12} \end{bmatrix} \tag{4}$$

This orthotropic compliance matrix contains nine unknowns [21]. These were estimated using the Cell Periodicity feature in COMSOL as well as with the (inverse) rule of mixtures. The results are shown in table 3 and show a good agreement between the two methods. The largest difference is found in the Poisson's ratios; in the rest of this work the values obtained from the FEM model are used.

The calculated elastic modulus E_1in the longitudinal direction is around 50% larger than that in the radial direction ($E_{2,3}$). The calculated thermal contraction of the winding pack in the filament direction $\Delta L_1/L_1$ is roughly the same as the value for stainless steel (−0.296% [18]), whereas in the radial directions it is in between steel and aluminium (−0.415% [18]).

4. Mechanical behaviour of the cassette

In this section the mechanical behaviour of the cassette surrounding the coils is described. First the requirements it needs to satisfy are introduced, followed by a discussion of the selected design, showing how it meets these requirements. Also, some inadequate designs are shown.

The enclosure of the coils needs to fulfil several functions:

(a) The coils need to be kept in place. The high current density and the strong magnetic field result in substantial Lorentz forces, which need to be contained so that the coils maintain their shape and position. In contrast to other superconducting systems, such as particle accelerators [33] or MRI magnets, a ppm accuracy in the magnetic field profile is not required for MDS. This is because the separation process is also influenced by factors such as poor wettability, turbulence and differences in feed particle sizes [1]. The concept of magnetic field quality in the context of MDS magnets in discussed in [14].

Table 3. Winding pack orthotropic material properties at 4.2 K, calculated using a FEM model of the unit cell (cell periodicity) and using the (inverse) rule of mixtures.

Property	Cell periodicity	Rule of mixtures
E_1 (GPa)	76	79
E_2 (GPa)	55	50
E_3 (GPa)	55	50
G_{23} (GPa)	21	19
G_{31} (GPa)	18	19
G_{12} (GPa)	21	19
ν_{21}	0.24	0.21
ν_{31}	0.24	0.21
ν_{32}	0.30	0.33
$(\Delta L_1/L_1)_{293\rightarrow 4\text{ K}}$ (%)	−0.303	−0.304
$(\Delta L_2/L_2)_{293\rightarrow 4\text{ K}}$ (%)	−0.349	−0.352
$(\Delta L_3/L_3)_{293\rightarrow 4\text{ K}}$ (%)	−0.349	−0.352

(b) The magnet and the ferrofluid attract each other. The enclosure needs to prevent the coils from moving a significant distance towards the fluid.

(c) The design needs to ensure that no mechanical energy release is possible with a magnitude sufficient to provoke a quench [24].

(d) The enclosure needs to provide a thermal connection between the cryocooler and the coils. This is important firstly to keep the static temperature difference between the winding pack and the cryocooler small, but also to obtain a reasonable cool-down time of the cold mass.

(e) The coils are not allowed to deform significantly due to gravity.

(f) The winding pack needs to be electrically insulated from the enclosure.

(g) The enclosure's thickness on the top of the coils increases the distance between coils and fluid, thus decreasing the gradient of the magnetic field magnitude at the fluid bed. It is crucial to minimize this thickness.

(h) The mass of the enclosure influences the required dimensions of the support structure that connects the cassette to the main body of the cryostat, and thus the conductive heat load on the cold mass. Secondly, the mass of the cassette influences the cool-down time. Over-engineering the mechanical strength of the enclosure thus has a negative effect on the thermal aspects of the system.

The MDS demonstrator cold mass design is the result of multiple iterations. First the final geometry is introduced. Designs that were investigated but did not meet all criteria are discussed in section 4.6. A schematic of the cold mass is shown in figure 5.

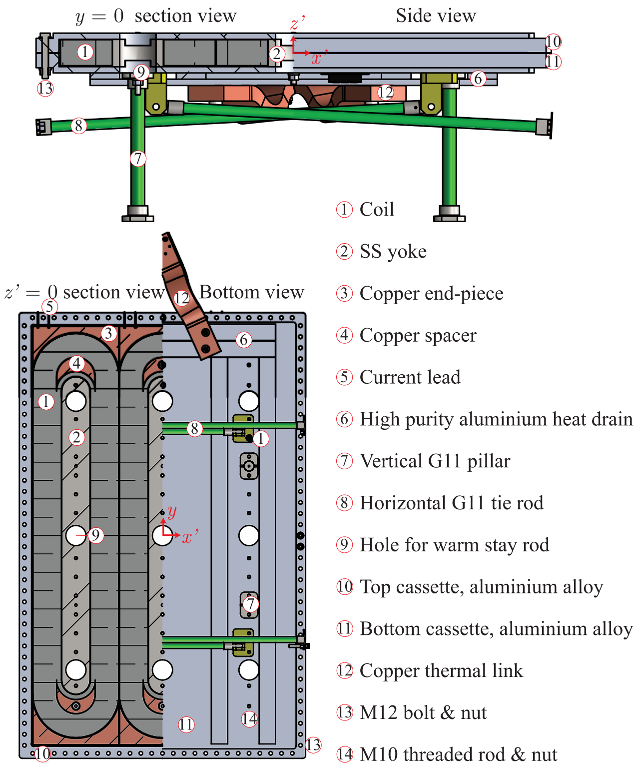

Figure 5. Schematic side view and bottom view of coils (1) and surrounding cassette. The cassette consists of two machined aluminium alloy plates (10,11), which are bolted together. Most of the bolts and nuts are not shown in the image. Underneath the bottom aluminium alloy part several high-purity aluminium heat-drain bars (6) reduce thermal gradients across the coils. The coils are wound around stainless-steel pole pieces (2) and have copper spacers (4) and copper end-pieces (3). Four vertical (7) G11 fibreglass pillars and four horizontal (8) G11 tie rods hold the cassette in place. Nine holes (9) in the yokes and cassette allow for the presence of room-temperature stainless steel columns, which help to reduce the thickness of the cryostat's flat plate. These columns are fixed to the same sliding plate as the vertical G11 pillars on the bottom side, and at the other side touch the cryostat flat wall. The stainless steel columns are not pictured in the figure. Also not shown are thin G11 plates on the top and bottom of the winding pack for electrical insulation.

The coils are enclosed in two aluminium alloy AL5083-H321 half cassettes, designated as top- and bottom plates, have a thickness of 12 mm at the thinnest sections. This thickness increases to 24 mm in certain sections in order to create enough length for M10 threads in the top plate. The stainless steel yokes have an H-profile cross-section to allow for this. M10 threaded rods and nuts connect the two aluminium plates. By using the threaded rod & nut solution the top plate of the cassette remains flat. A ring of M12 bolts surrounds the cassette. Here there is space to use a bolt-and-nut configuration (see the top-left of figure 5). The bolted connections are discussed in more detail in section 4.4.3.

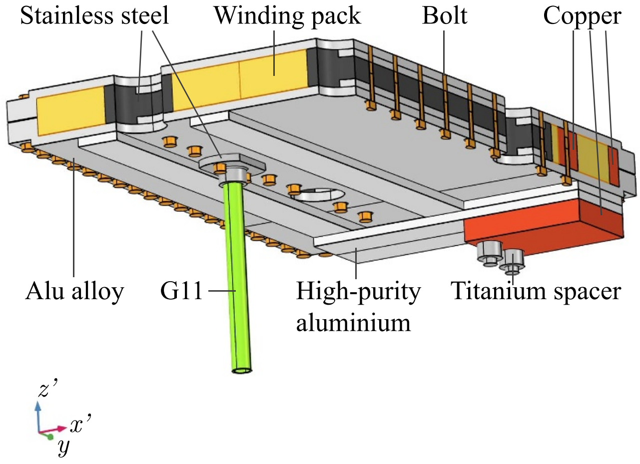

Figure 6. Simulation geometry, consisting of a quarter of the cold mass. Coils and stainless steel yoke are enclosed by two aluminium alloy parts, connected by steel bolts. Also shown are copper crescents and end-pieces. Copper is chosen for these parts due to its high thermal conductivity and because its thermal contraction is close to that of the winding pack. Underneath the cassette pure aluminium heat drain bars are present, as well as a copper block representing the link between the cryocooler and the cold mass. This block is pressed to the bars by using a combination of steel bolts and titanium spacers. A vertical G11 pillar is connected to the bottom cassette part via a stainless steel fixture.

Four vertical and four horizontal G11 pillars hold the cassette in place on the sliding plate below. These pillars are optimized to balance mechanical strength with the heat in-leak through conduction. Depending on the loading scenario (room-temperature magnet, energized magnet with full fluid bed, energized magnet with partially-filled fluid bed) they can be loaded in tension or in compression. Section 5 deals with these pillars.

To remove the heat load on the cassette, high-purity aluminium heat drain bars with RRR $>$1500 are attached underneath the cassette. These are glued in place using Stycast 2850FT epoxy resin, since the thermal contact is not critical due to the large contact area. For more details on thermal aspects the reader is referred to [15]. A copper thermal link connects the aluminium bars to the cryocooler. This link is flexible to allow cool-down of the system without applying a significant mechanical load on the cryocooler due to thermal contraction.

The coils are fitted inside the cassette using stainless steel shims.

The coils are wet-wound using Stycast 2850FT. This specific epoxy was selected because it has a thermal expansion coefficient that is relatively close to that of the conductor.

The Lorentz forces contribute the largest force on the coils that needs to be contained. In section 4.6 we introduce several unsuccessful concepts, most of which also rely on the use of an aluminium alloy casing to provide a pre-compression force during cool-down due to the alloys large thermal contraction.

4.1. Simulation geometry

The mechanical calculations on the cold mass were performed using COMSOL Multiphysics. The simulation geometry consists of a quarter of the cold mass and is shown in figure 6. The geometry represents the upper left quadrant of an

$x'y$-symmetry plane. The assumption is made that the mechanical load on this quarter in combination with symmetry boundary conditions accurately represents the whole cold mass. As a simplification the 12° angle is neglected. Thus, gravity is directed perpendicular to the coils' surface (in $-z'$). By considering this specific quarter of the geometry, the presence of the high-purity aluminium heat-drains running in the x'-direction is amplified.

In the simulation geometry only the vertical G11 pillar is considered, to verify the effect of the ferrofluid-coil attraction on the displacement of the cold mass and to analyse the glued connection between the pillar and its fixture. The horizontal G11 tie rods are assumed to have a low stiffness in the vertical direction as motivated in section 5, and are not modelled in this specific simulation.

The coils are modelled as composites with homogeneous orthotropic mechanical properties, as derived in section 3. To allow for this anisotropy a curvilinear coordinate system is defined with a principal axis in the direction of the current in the coils.

4.2. Contact conditions

The components form an assembly in which relative movement of boundaries is possible depending on the settings. The boundary contact types between the different component are

- Contact. Boundaries may have a gap between them, and when touching a contact pressure can be present. For the contact between the sides of the cassette and the outer flat sides of the winding pack, a 0.1 mm initial offset is put to represent imperfect shimming. For the connection between the bottom cassette and the stainless steel fixture holding the G11 pillar, a friction coefficient of 0.3 is added. This is required to prevent free motion of the pillar and fixture in the $x'y$-plane;
- Thin elastic layer. This layer represents the thin G11 plates that are on top (0.5 mm thick) and bottom (2 mm thick) of each coil. The Young's modulus of this layer is set to 20 GPa [18]. This method avoids the need to mesh the thin plates;
- Glued. The glued layer reflects the epoxy connection between boundaries; adhesion between layers takes place at room temperature for boundaries of this type as long as their initial distance is less than 0.5 mm. The glue has a elastic modulus of 24 GPa [25]. The main difference with the thin elastic layer boundary is that the glued boundary can break if either the tensile strength or the shear strength of the epoxy is exceeded. In the simulation the tensile strength is set to 100 MPa at 77 K and 42 MPa at 300 K [37]. Interpolation is set to linear and extrapolation to constant. The shear strength is similarly set to 32 MPa at 77 K and 18 MPa at 300 K [37].
- Continuity. This represents boundaries that can be considered fixed to each other. An example is the simplified representation of threaded connections.

4.3. Loads

The following loading paths are considered in the simulations:

- First, gravity, pre-stress due to winding tension and pre-stress due to bolt tightening are applied. The whole geometry is kept at room temperature. Gravity is applied as a body load to each component. The bolt tightening is applied using COMSOL's bolt pre-stress feature. The correct method of applying the pre-stress resulting from winding the coils was validated first with a solenoid, as for this case an analytical formula is available to verify the result [39]. The pre-stress in the COMSOL model was applied by enforcing an initial stress in the azimuthal direction. The agreement with the analytical solution was sufficient to conclude that also on the racetrack coils the pre-stress can be approximated by applying an initial stress of 50 MPa (determined by the winding tension) in the direction of the wire. The same curvilinear coordinate system used to apply the anisotropic material properties is used. Also taken into account is the stress resulting from compressing the coil during the curing of the Stycast in the manufacturing process. This pressure is exerted on the straight section of the racetracks and is estimated to be 5 MPa.
- Second, the cold mass is cooled down to 4.5 K. This is simulated in steps so that the stress in the epoxy layer between the G11 pillar and its steel fixture can be checked for damage due to differential thermal contraction, over the entire temperature range.
- Third, the Lorentz forces are applied to the winding packs as a body force on the composite using the results of a 3D FEM magnetic field calculation. The total horizontal Lorentz forces on the quarter of the winding packs (figure 6) are 489 kN in the $-x'$-direction and 290 kN in $+y$ [13].
- Last, the attraction force between coils and ferrofluid is applied as a body force. The worst-case scenario of 34 kN is taken corresponding to an unstable ferrofluid in which the nanoparticles agglomerate near to the bottom of the bed [34]. In the remainder of the section, when the magnet is considered energized this means that the Lorentz force as well as the fluid attraction force are taken into account. Note that in reality the attraction force and the Lorentz force are likely to ramp up simultaneously. This is the case when the magnet is energized while the ferrofluid is present above the magnet and in the normal operation.

4.4. Simulation results

4.4.1. Aluminium alloy cassette. The largest stress in the aluminium cassette is situated around the holes in the cassette for the room-temperature stainless steel columns that support the cryostat top plate. The von Mises stress in the cassette after energizing is shown in figure 7. The peak stress increases from 174 MPa after cool-down to 197 MPa after applying the Lorentz force. This is around 72% of the yield stress of the alloy at 4.2 K (275 MPa [35]) and slightly higher than the factor 2/3 initially aimed for. The 197 MPa is 34%

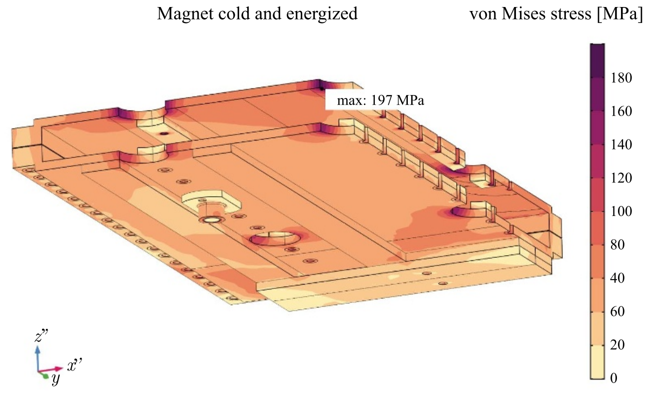

Figure 7. Von Mises stress in the aluminium cassette after cool-down of the cold mass and energizing.

of the 572 MPa ultimate tensile strength of AL5083 H321 at 4.2 K [36].

While local plastic yielding of the cassette could in principle be allowed, the gain in performance, that is, of the vertical magnetic field gradient at the fluid bed, by reducing the cassette thickness is small (at most 12%). For a more powerful magnet, i.e. one that generates higher Lorentz forces, a more aggressive cassette design (i.e. allowing local plastic yielding) might be beneficial. However, reducing the cassette thickness would also reduce the applied compression on the coils during cool-down, as further discussed in section 4.5.

The high-purity aluminium bus bars see a stress of 40 MPa. Since the yield strength of pure aluminium is as low as 35 MPa [18], some plastic yielding of the bars can occur. This non-linear stress–strain relation is not taken into account in the model. The maximum stress in the Stycast glue layer between the bars and the cassette is below 30 MPa, well below the yield strength [37].

A question that arises in view of the stress concentration around the holes is whether using such a stainless steel column structure is indeed preferred.

The deflection of the cryostat top plate scales with the top plate thickness as d^{-3}, as seen in equation (3). In combination with the results from section 2, it is estimated that the cryostat top plate, if unsupported by columns, needs a thickness of 43 mm to obtain the same deflection as a 20 mm supported plate. Thus the gain of using the column structure for the cryostat thickness is at least 23 mm whereas the cassette is only 12 mm thick. The issue of whether these columns also make sense for more powerful MDS magnets is addressed in section 4.5.

4.4.2. Winding pack. The computed displacements of the winding packs are shown in figures 8(a)–(c) in the directions x', y and z'. Three scenarios are presented: (1) The initial room-temperature situation including winding pre-tension, gravity and tightening of the bolts, (2) cool-down to 4.5 K, and (3) energizing the magnet with a ferrofluid present above it.

The shrinkage of the cold mass in the x'-direction shows almost no variation with the y-direction. Likewise the displacement in y shows almost no variation in x'. Thus it is concluded that the aluminium cassette behaves as a rigid body during the shrink-fit.

The relative displacement of the winding pack in the x'-direction towards the origin is 0.369%, in the y-direction 0.353%. It makes sense that the shrinking in the y-direction is somewhat less when considering that the transverse thermal expansion of the unconstrained winding pack is -0.352% compared to -0.304% in the longitudinal direction (table 3). The calculated values of the constrained winding pack are in between those of the unconstrained winding pack and of the empty cassette (-0.415%).

In the z'-direction the cold mass moves downwards because the G11 pillars to which the cold mass is attached are fixed at the bottom. The magnitude of this displacement is exaggerated because the whole pillar is cooled to 4.5 K in this simulation. In reality one side of the pillars is attached to the room-temperature cryostat whereas the other is attached to the 4.5 K cold mass. A 1D FEM calculation estimates the heat-sinked vertical pillars to shrink 0.5 mm.

As for the variation of the z'-displacement with the x'- and y-coordinates, some bending (0.6 mm) of the coils takes place. This is the consequence of the presence of the aluminium bars on the bottom of the cassette that allow the bottom cassette to pull on the winding pack harder than the top cassette.

During the energizing of the magnet the Lorentz force tries to expand the coils. In the x'-direction the cold mass is rigid enough so that no large deformation takes place. The same holds for the displacement in the y-direction. In the z'-direction, however, the coils moves half a millimetre towards the ferrofluid. This counteracts the expected movement during cool-down.

The von Mises stress in the winding packs is shown in figure 8(d). The maximum (89 MPa) is found in the inner section of the heads after cool-down. This decreases to 83 MPa after the magnet is turned on.

The different stress components are shown separately in figure 9. From figure 9(a) it can be seen that a tensile longitudinal stress is present at room temperature, caused by the winding tension. After cool-down this stress component mostly disappears due to the shrink-fit of the cassette. When energizing the magnet the longitudinal stress increases, with a maximum at the inner radius of the bent sections of up to 40 MPa. Assuming parallel loading of the composite in the direction of the current, the rule of mixtures can be applied to estimate the longitudinal stress in the different components of the winding pack. This leads to an estimated 12 MPa tensile stress in the epoxy, which is well below the yield strength in tension of more than 100 MPa of Stycast 2850FT at 4.2 K [37]. NbTi/Cu superconductor can handle up to 500 MPa in tension before a significant degradation of the superconducting properties occurs [24] so that a large safety margin is present.

In the transverse direction[1], see figure 8(b), the winding pack sees an initial small compression at room temperature due to the winding tension, and a large increase in compression

---

[1] Taken here as the direction perpendicular to the conductor in the $x'y$-plane.

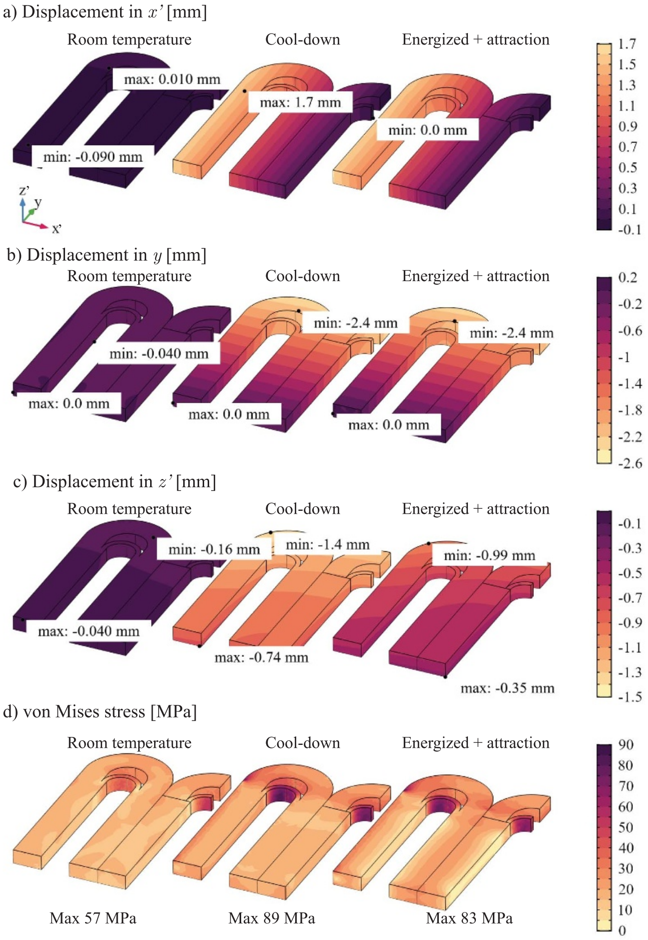

Figure 8. Simulation results of the displacement of the winding packs. (a)–(c) refer to the displacements in directions x', y and z' respectively; (d) shows the von Mises stress.

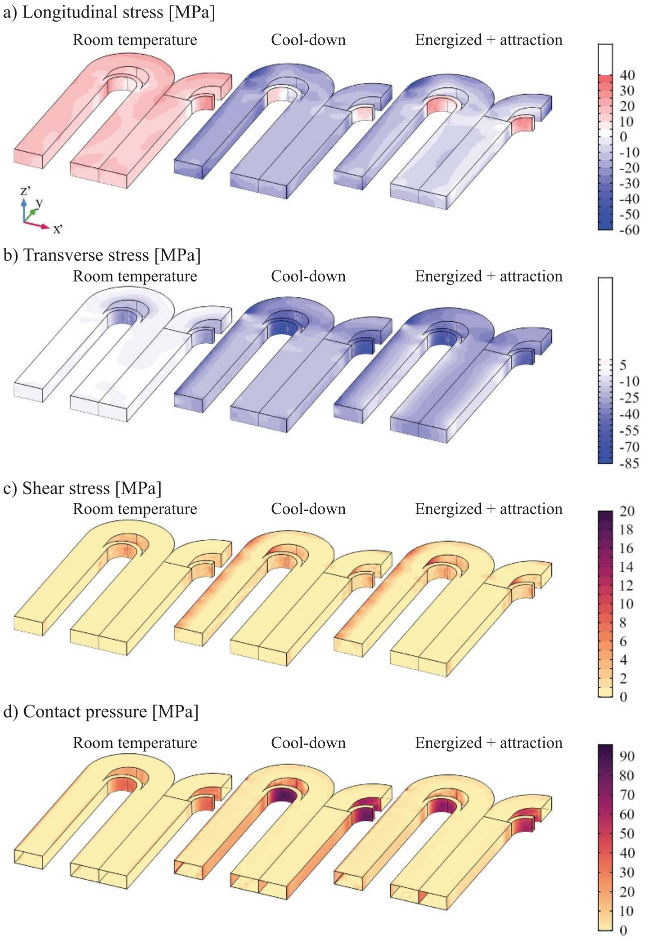

Figure 9. Simulation results of stresses in the winding packs: (a) Longitudinal stress; (b) Transverse stress; (c) Shear stress. (d) Contact pressure.

during cool-down. When the magnet is energized part of the compression is relaxed. The magnetic forces are not sufficient to cause a positive transverse stress in the composite winding pack. A negative transverse stresses reduces the formation and propagation of cracks in the epoxy, and the release of mechanical strain in the form of heat that is associated with these cracks, and is thus required [23] for LTS magnets. Thus the aluminium cassette is thick enough as far as the pre-compression is concerned.

The maximum shear stress at the interface between coils and the stainless steel yokes, see figure 9(c), is 7 MPa. This shear stress would be higher if this connection would be glued. A Teflon coating applied to the steel yoke before winding allows for the free relative movement of the components. The copper crescent spacers, see figure 5, are however glued in the winding pack and a shear stress of up to 14 MPa develops in the outer heads of the winding packs at this interface. This remains below the epoxy's shear strength of 32 MPa at 77 K [37].

The coils stay in contact with the steel yokes after energizing. The maximum contact pressure of 85 MPa occurs after cool-down, see figure 9(d), and reduces by around 20 MPa after excitation.

4.4.3. *Clamping the coils—bolts & threaded rods.*

Next we focus on the simulation of the cold mass as a whole. The two cassette parts need to be attached to each other in order to keep the coils in place and to maintain contact. This is achieved by using an array of 128 stainless steel M12 bolts surrounding the coils, and by 48 stainless steel M10 threaded rods that run along the y-centreline of each coil. Figure 10(a) shows a schematic representation of the bolts and threaded rods. To minimize the required computational effort, the geometry is simplified as shown in figure 10(b).

Perhaps counter-intuitively, the tensile load on the bolts and threaded rods increases significantly during cool-down, from 30 to 130 MPa depending on the bolt location. This is caused by the higher thermal expansion coefficient of the aluminium alloy compared to the winding pack (aluminium shrinks -0.415%, stainless steel -0.296% and the winding pack -0.303 to -0.349%, see section 3). In other words, the cassette 'wants' to shrink more than the coils. Thus, the outer parts of the cassette are pulled apart, as illustrated in figure 10(c). The bolts keep the two cassette parts together, resulting in the increased tensile stress on the bolts, see figure 10(d). Since the length-scales of interest in the $x'y$-plane are much bigger than the length of the bolts, differential

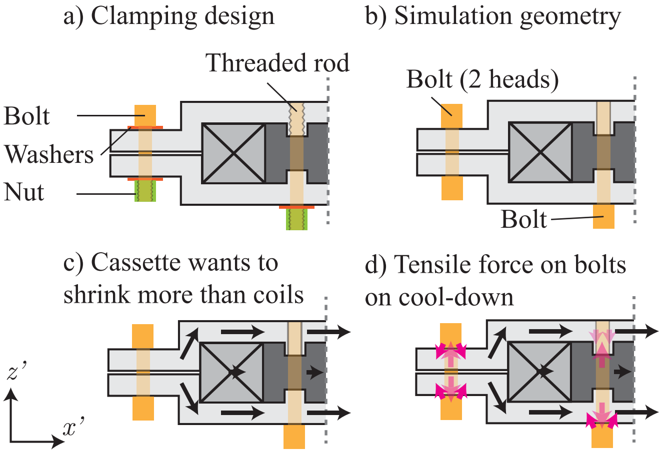

Figure 10. (a) Schematic of the method used to fix the cassette to the coils. Around the cassette, bolts and nuts keep the two aluminium alloy parts together. Through the yokes of the coils threaded rods are present, fixed in threads in the top cassette and by nuts underneath the bottom cassette. (b) This geometry is simplified in the mechanical simulations; the outer bolts and nuts are modelled by bolts with two heads. The threaded rods are represented by a bolt, fixed to the top cassette by a simplified thread. The washers are represented by increasing the bolt head thickness. (c) During cool-down the two cassette halves try to pull themselves away from each other, as they shrink towards the x'-symmetry plane. (d) This results in a tensile load on the bolts.

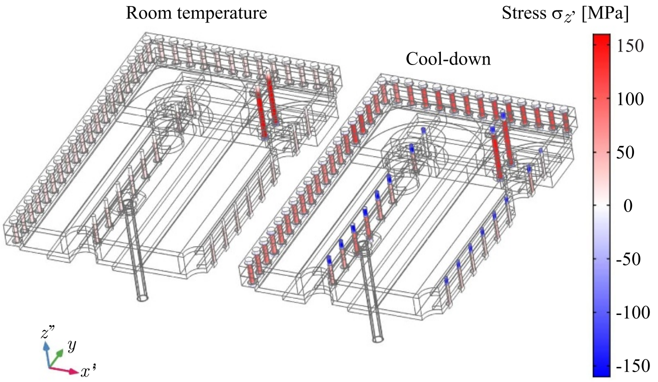

Figure 11. Stress in the bolts in longitudinal direction z' after pre-tensioning at room temperature and after cool-down.

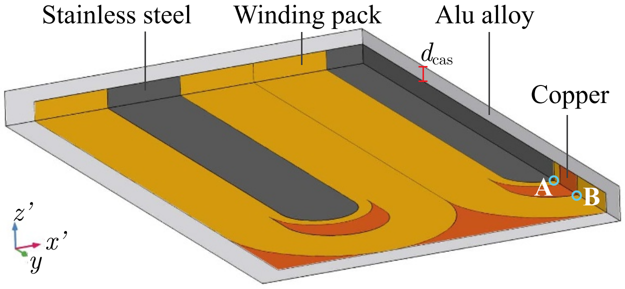

Figure 12. Simulation geometry, consisting of an octant of the cold mass. The copper pieces and winding packs are glued together. The winding pack and the aluminium have a contact boundary condition.

thermal shrinking in the z'-direction does not play a significant role.

The stress in the bolts is shown in figure 11. To ensure that the bolts see approximately the same load during cool-down, a pre-stress is applied to the bolts at room temperature of around 20 MPa. However, the bolts connecting the thermal link to the cassette are pre-stressed to 160 MPa as the clamped connection between the thermal link and the cassette benefits from a high force. This link and the interface with the cold mass is discussed in more detail in [15]. Titanium spacers are used between the bolt heads and the thermal link to ensure that this pre-tension is not lost during cool-down, since the stainless steel bolts have a relatively low thermal contraction coefficient. Since titanium has a thermal contraction coefficient even lower than that of stainless steel [18], nevertheless the bolts remain in tension.

4.5. Effect of cassette thickness

In this section the influence of the cassette thickness is presented on (1) the transverse compression of the winding pack during cool-down, (2) the longitudinal stress in the winding pack and (3) the stress in the cassette itself. All these are obtained from COMSOL simulations. The geometry of the cold mass is simplified to keep the calculation time acceptable. It consists of an octant of the geometry, see figure 12. The aluminium cassette is simplified to a single solid piece. Perfect shimming of the coils in the cassette is assumed, i.e. there is no offset between boundaries at room-temperature. The effect of winding tension, which is beneficial for the transverse stress and unwanted for the longitudinal stress, is not considered. The longitudinal stress is evaluated in point A in figure 12, since it is the highest at this location and also the magnetic field is highest here. The transverse stress is evaluated at point B. The magnetic field is of similar magnitude at this point.

A parametric study is performed where the thickness of the aluminium alloy cassette is swept from 12 to 100 mm. For each thickness, a simulation is performed that starts with a calculation of the thermal stress, followed by applying a Lorentz force of various magnitudes. The electromagnetic forces range from 0.5 to 8 times the Lorentz force level experienced by the NbTi demonstrator during normal operation, F_{L0}.

In figure 13 the transverse stress in the winding pack is presented as a function of the cassette thickness. The stress is negative after cool-down due to the differential thermal contraction and increases in magnitude with increasing cassette thickness. The Lorentz force increases this stress, with a magnitude that seems to be fairly independent of the cassette thickness. It was chosen to maintain a negative (compressive) transverse stress to prevent tension on the epoxy, thus these simulations are used to estimate the minimal cassette thickness required to handle a certain Lorentz force.

In figure 14 the longitudinal stress in the winding pack is plotted as a function of cassette thickness. The cool-down results in a longitudinal compression of around −14 MPa, virtually independent of the thickness of the aluminium cassette.

Upon applying an electromagnetic body force to the winding packs equal to that of normal operation, the longitudinal

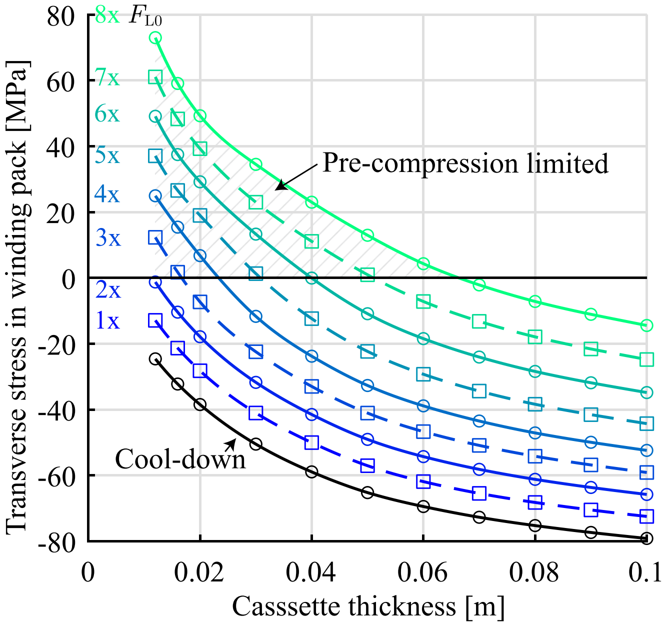

Figure 13. Transverse stress (in $x'y$-plane) in the winding pack as a function of cassette thickness d_{cas}, see figure 12, plotted for different Lorentz force levels, indicated by different colours. These levels are relative to the NbTi demonstrator (F_{L0}). Data-points are indicated with markers. The hatched area indicates load-cases in which the winding pack in under positive (tensile) transverse stress.

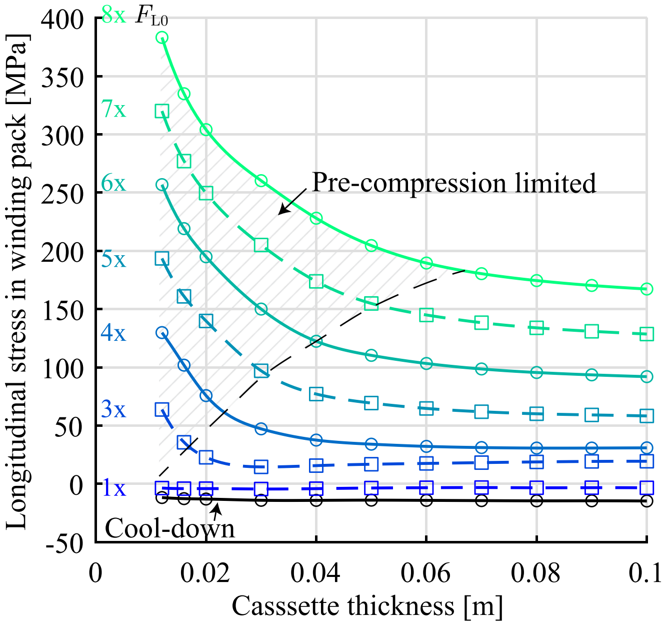

Figure 14. Longitudinal stress in the winding pack as a function of cassette thickness d_{cas}, see figure 12, plotted for different force levels, indicated with different colours. Data-points are indicated with markers. The hatched area above the dashed line indicates load-cases in which the winding pack in under positive (tensile) transverse stress.

stress increases to around -4 MPa. A further increase of the force level results in an increase of the stress that depends on the thickness of the cassette. NbTi/Cu conductor can handle a tensile stress of 500 MPa [24]. With an estimate that the uninsulated conductor occupies 68% of the winding pack volume, a maximum still reasonable winding pack longitudinal stress of 340 MPa is found. Only at force levels of upwards of 7 times that in the demonstrator, in combination with a thin cassette, is this value approached. However, such a low cassette thickness does not provide enough pre-compression to prevent positive transverse stresses, as explained in the context of figure 13. The minimum thickness corresponding to a certain Lorentz force level is indicated with a dashed black line in figure 14.

Thus, it was concluded that the longitudinal stress component is not a major factor in determining the minimum winding pack thickness for NbTi MDS magnets.

If the cassette is relatively thin, the winding pack dominates the thermal shrinkage of the cold mass, and if it is thick, the cassette dominates. Thus during cool-down a tensile stress develops in the cassette that decreases with increasing cassette thickness.

The von Mises stress in the aluminium is shown in figure 15. This stress is estimated by multiplying the stress in the solid bulk (figure 12) by a factor three to obtain the stress concentration around the holes, see figure 7, that allow the room-temperature columns to pass through. The assumption is made that this factor three between the stress in the bulk of the aluminium and the stress concentration around the holes is independent of the thickness of the cassette.

The minimum thickness that provides sufficient transverse pre-compression corresponding to a certain Lorentz force level is indicated with a dashed black line in figure 15. The maximum stress is about the same as for the demonstrator. Higher stress levels might also be allowed as far as the aluminium is concerned, since aluminium alloys exist with a yield strength of at least 700 MPa at cryogenic temperatures, for example 7175-T4 with 745 MPa and 7075-T6 with 750 MPa [35].

In conclusion, the stress in the *cassette* is not a limiting factor in the performance (i.e. the distance between the coils and the ferrofluid). Thus, removing the holes that allow the room-temperature columns would not bring any advantages as far a the required cassette thickness is concerned. The columns are therefore a good solution for not just the demonstrator but also for more powerful MDS magnets.

A second conclusion is that the main factor determining the minimum cassette thickness is the amount of pre-compression applied by the cassette due to differential thermal shrinkage during cool-down.

Another conclusion is that very high strength aluminium alloy is not required.

As a thicker cassette implies a larger distance between the coils and the ferrofluid, it is of interest to consider designs that do not require the presence of a strong cassette on the fluid facing side of the magnet. Several such concepts are presented in the next section.

4.6. Asymmetric cassette design attempts

In this section a few earlier concepts for the mechanical design are presented, which were explored but found unsuitable. Three concepts were conceived aiming to handle

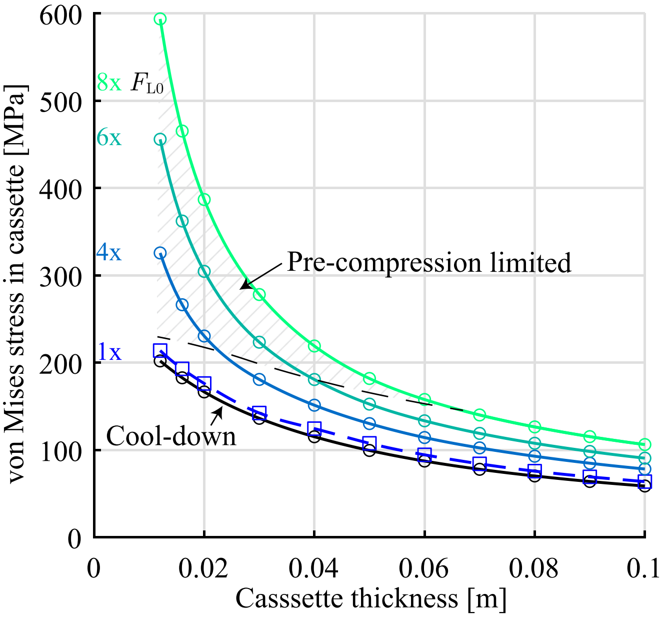

Figure 15. Von Mises stress in the aluminium alloy cassette as a function of cassette thickness d_{cas}, see figure 12, plotted for different force levels. Data-points are indicated with markers. The hatched area indicates load-cases in which the winding pack in under positive (tensile) transverse stress.

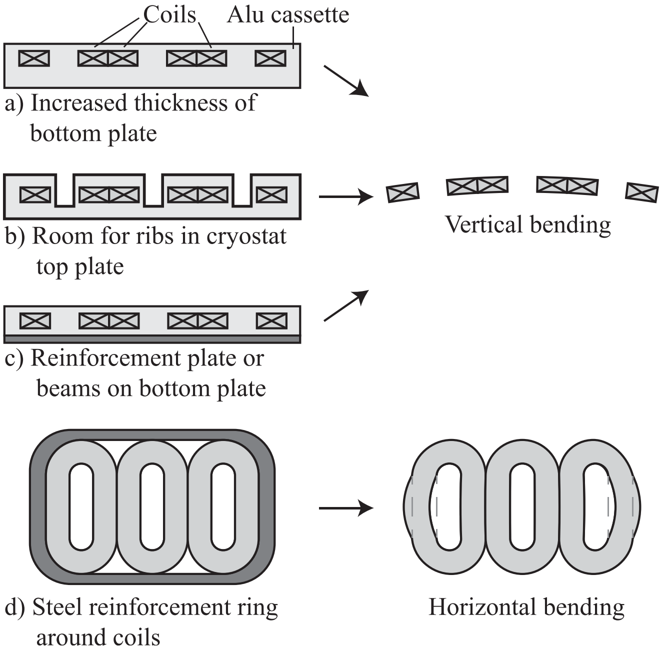

a) Increased thickness of bottom plate

b) Room for ribs in cryostat top plate

c) Reinforcement plate or beams on bottom plate

d) Steel reinforcement ring around coils

Figure 16. Compilation of concepts to reduce the coil-to-fluid distance with no satisfactory results. (a) Increasing the thickness of the bottom part of the cassette results in vertical bending of the coils, due to asymmetric contraction during cool-down. (b) Cutting out part of the top of the cassette enables the use of a ribbed, thus stronger, cryostat plate, but also results in too much bending. (c) Reinforcing the cassette on the bottom by using stiff beams also is not useful. (d) Making use of the space on the sides of the coils by using a reinforcement ring leads to in-plane bending, as the ring is not stiff enough due to the long arm over which the Lorentz force has to be transferred.

the Lorentz forces by using the space available below the coils, thus reducing the thickness of the cassette at the top-side and hence also the fluid-magnet distance. These are schematically depicted in figures 16(a)–(c). A fourth concept was to enclose the coils in a steel reinforcement ring, see figure 16(d).

The first, most simple approach taken was to increase the thickness of the mechanical cassette only of the bottom, as shown in figure 16(a). However, this caused a significant bending of the winding pack, since the thermal contraction of the bottom plate exerts a stronger force than the top plate, resulting in asymmetric tension on the winding pack.

The second option, illustrated in figure 16(b), utilizes slits between the coils, to allow for reinforcement ribs on the cryostat top plate. Similar bending as in the previous design is found, as the asymmetric contraction is still present.

In an attempt to neutralize the effect of the asymmetric contraction, a material with a low thermal contraction coefficient could be attached to the bottom of the cassette, see figure 16(c). Ti-6Al-4V has a thermal contraction of only 0.173% between room temperature and 4.2 K, but a relatively average Young's modulus of 114 GPa and it is prone to brittle fracture at high stress levels [18]. A different material option could be Hastelloy C-276, with a thermal contraction of 0.218% and Young's modulus of 205 GPa [18]. Alternatively, one might even consider a ferromagnetic material, such as FeNi, with 0.195% contraction for Fe-9%Ni [18]. An additional benefit would be a reduced stray magnetic field around the magnet (the 0.5 mT line is at around 3.5 m from the centre of the demonstrator).

Simply using a flat plate bolted to the aluminium alloy base plate has the downside that the thermal contraction force is not equal in the two horizontal directions. Thus the coils still see an asymmetric force causing them to bend. One would need to resort to a ribbed structure to equalize the thermal contraction in both horizontal directions.

A further idea was to enclose the coils in a reinforcement ring, see figure 16(d). At first sight, this symmetric approach looks promising since no vertical bending of the coils is present. However, even a 0.20 m thick steel ring was found to lack the required stiffness to prevent horizontal bending. The effective moment caused by the Lorentz force in the x'-direction is large as a result of the long arm. Moreover, this type of mechanical enclosure results in a high tensile stress of some 300 MPa in the coil heads.

From the four options only the third one (figure 16(c)) shows some potential for further exploration. The gain of in magnetic field gradient would be about 13% for the demonstrator. This is the effect of subtracting the cassette top plate thickness of 12 mm from the coil-to-fluid distance. The loss in performance due to the symmetric design is considered acceptable in view of the higher simplicity of the mechanical structure for the demonstrator magnet. As detailed in [13], however, the performance of high-field MDS magnets can be significantly improved if a suitable asymmetric mechanical design can be found.

The idea of placing magnetic iron underneath the coils to help boost the magnitude of the magnetic field was discarded early on in the design process in order to have more

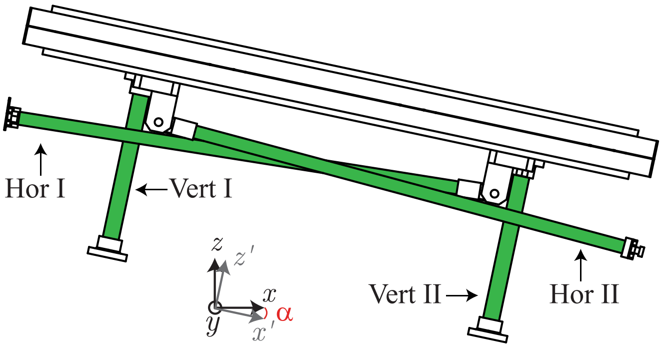

Figure 17. Side view of the cassette that encloses the coils and of the pillar structure suspending it inside the cryostat. The structure consists of four solid horizontal tie-rods (two 'Hor I' and two 'Hor II') and four vertical hollow pillars ('Vert I' and 'Vert II'). They are made from G11 fibreglass tube and the tube ends are glued in stainless steel sockets.

freedom in the design to meet the mechanical- and thermal requirements of the magnet. A 'back-iron' underneath the coils would take up space that is now available for the cassette, high-purity thermal bus, instrumentation, and assembly access. Also, the added weight of the iron was considered unattractive as it would require increasing the strength of the warm-cold support structure and hence an increased heat in-leak. Thus iron was excluded from the design essentially for simplicity.

5. Cold mass support structure

5.1. Introduction

This section concerns the design of the G11 structure that hold the MDS cold mass in place. Since these pillars are at room temperature on one side and at cryogenic temperature at the other, they will be referred to as *warm-cold pillars*.

The warm-cold pillars are shown in figure 17 and are made up out of four hollow tubes (z' oriented and indicated as 'vertical'), and four solid tie-rods (indicated as 'horizontal'). A schematic is shown in figure 17. Two of these tie-rods are placed in the x'-direction with a $+3°$ angle offset in the $x'z'$-plane, and two at $-3°$. We will assume that they are actually oriented in the x'-direction, neglecting the 3° offset.

In the design of the pillar structure, a trade-off is made between heat in-leak, requiring a small cross-sectional area of the pillars, and strength against buckling, requiring a certain minimum cross-section. A safety factor of four was chosen to determine the tube size and wall dimensions. Furthermore, upon energizing, the pillars may—depending on the position and scenario—also become loaded in tension.

First the critical buckling load is considered and next the heat in-leak through the pillars. Then, a figure-of-merit is introduced to compare materials to find the best pillar material optimized for high buckling strength and low heat in-leak. It was found that G11 is the optimum practical material. Additionally, the pillar design is checked for tensile strength, since it is required to handle the attraction force between ferrofluid and coils. These analytical calculations are compared to FEM simulation results.

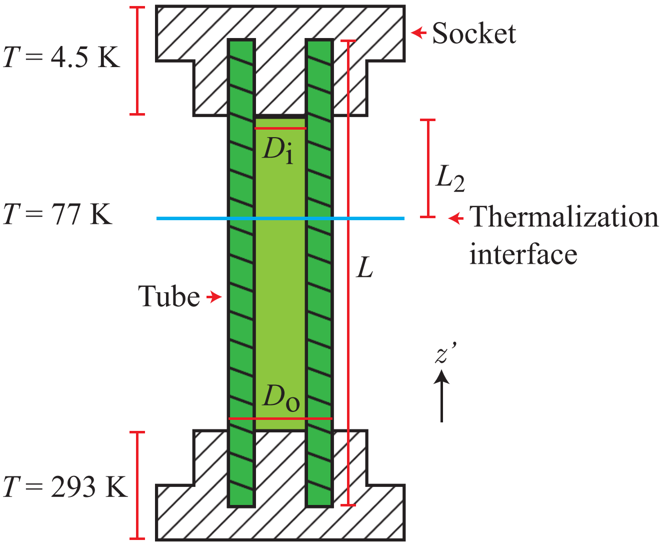

Figure 18. Cross-section of a G11 hollow pillar with length L, inner diameter D_i and outer diameter D_o, as well as two sockets. The aim of the pillar is to separate the cold mass from the cryostat bottom plate with minimal heat in-leak. The fixtures, made from stainless steel 304, are considered to be at a uniform temperature, since their thermal conductivity is around 20 times higher than that of G11 [18] both at 4.5 K and at room temperature. The tube is thermalized at an intermediate temperature of around 77 K by a connection to the thermal shield, at a distance L_2 from the cold end [15].

5.2. Buckling: critical load

Euler's buckling criterion for a tube determines that buckling will occur once the compressive load exceeds a certain critical value F_cr [18]:

$$F_\mathrm{cr} = \frac{C\pi^3 E}{L^2}\frac{\left(D_\mathrm{o}^4 - D_\mathrm{i}^4\right)}{64}, \tag{5}$$

where E is Young's modulus, L is the length of the pillar, and D_o and D_i its outer- and inner diameters of the tube, respectively. The constant C in the buckling criterion depends on the boundary conditions of the loading. A worst-case value of 0.25 is assumed [18].

The critical load can be seen as the gravitational load F_z on each pillar, times a safety factor of N:

$$F_\mathrm{cr} = \frac{NF_z}{n}. \tag{6}$$

Here n is the number of pillars and the 12° angle between the z'- and z axis is neglected.

The heat in-leak to the cold end of n tubes is given by:

$$\dot{Q}_\mathrm{c,total} = \frac{n\bar{k}\Delta T}{L_2}\frac{\pi}{4}(D_\mathrm{o}^2 - D_\mathrm{i}^2), \tag{7}$$

where L_2 is the distance between the cold end of the pillar and the heat sink, as illustrated in figure 18. The heat sink temperature is set to 77 K in the calculations. $\bar{k}$ is the effective heat conductivity coefficient, determined by a thermal conductivity integral, for the temperature gradient across this section of the pillar ($\Delta T = 77\ K - 4\ K$).

The total heat in-leak of n pillars that can withstand buckling, including the safety factor N, is obtained by solving equation (5) for D_o and filling this expression in equation (7):

$$\dot{Q}_{\mathrm{c,total}} = \frac{n\bar{k}A\Delta T}{L_2}\frac{\pi}{4}\left[\sqrt{\left(\frac{64NL^2F_z}{nC\pi^3E}+D_\mathrm{i}^4\right)}-D_\mathrm{i}^2\right]. \qquad (8)$$

In the case of a solid rod ($D_\mathrm{i} = 0$), this reduces to:

$$\dot{Q}_{\mathrm{c,total}} = 2\bar{k}\Delta T\frac{L}{L_2}\sqrt{\left(\frac{NnF_z}{C\pi E}\right)}. \qquad (9)$$

A figure of merit (FOM) is defined to compare materials to be used for the pillars. Equations (8) and (9) indicate that the heat in-leak is minimized by minimizing $\bar{k}/\sqrt{E}$. Therefore,

$$FOM \equiv \frac{\bar{k}}{\sqrt{E}}. \qquad (10)$$

Note that the length of the pillar does not influence the heat in-leak at 4.5 K, only the relative placement of the radiation shield L/L_2 is important[2]. With the number of pillars the heat in-leak increases as well. Hence it is more optimal to use a few relatively thick pillars than many thin ones.

Between 4.5 K and 77 K, the effective thermal conductivity is 0.21 W/m/K for G11 and 4.5 W/m/K for SS304 stainless steel, calculated using thermal conductivity integrals [18]. Young's moduli at room temperature are 20 GPa for G11 and 195 GPa for SS304 steel, respectively [18, 38]. This gives:

$$FOM(\mathrm{G11}) = \frac{0.21}{\sqrt{20}} \approx 0.047, \qquad (11a)$$

$$FOM(\mathrm{SS304}) = \frac{4.5}{\sqrt{195}} \approx 0.32. \qquad (11b)$$

G11 thus allows to reduce the heat in-leak by a factor 7 compared to SS304 when using rods. The next section concerns the attainable reduction in heat in-leak by using hollow tubes.

5.3. Optimized pillar dimensions against buckling

Equation (8) is used to relate the diameter of the warm-cold pillars to the heat in-leak for a gravitational load of 5 kN. A conservative safety factor of four is included. The result is shown in figure 19, for a 4-pillar G11 design, and in figure 20 for four SS304 pillars. The heat load is summed for all four pillars. The thermal heat sink is connected at $L_2 = 0.37L$ [15]. The length of the pillars is set to 0.272 m. Even though increasing L_2 decreases the in-leak at the cold side, in this case the need for accessibility during assembly did not allow a larger distance between heat sink and cassette.

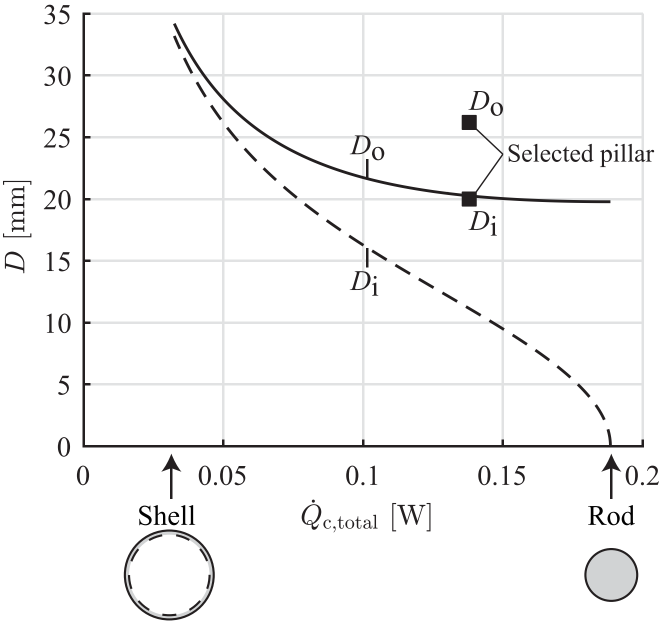

Figure 19. Relation between the inner- and outer diameters of the pillars and the heat load through four pillars at 4.5 K, $\dot{Q}_{\mathrm{c,total}}$, for a four-pillar G11 configuration with $L_2 = 0.37L = 100$ mm, see figure 18. The heat load and diameters are linked through the required resistance against buckling. The selected pillars have an inner diameter of 20 mm and an outside diameter of 26.2 mm and are indicated by black square markers. It can be seen that these pillars are somewhat over-dimensioned.

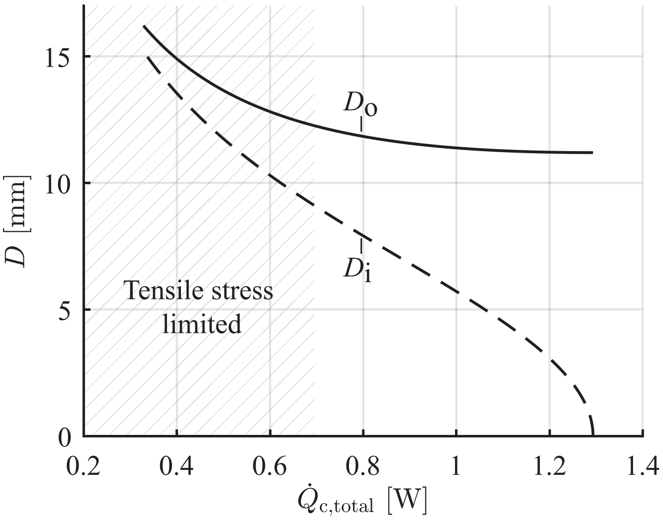

Figure 20. Relation between the inner- and outer diameter of the pillars and the heat load through four pillars at 4 K, $\dot{Q}_{\mathrm{c,total}}$, for a four-pillar SS304 configuration with $L_2 = 0.37L$, see figure 18.

The solid line shows how the outer diameter of the pillar needs to increase to reduce the heat load. The inner diameter is shown by the dashed line. The pillar quickly becomes thin-walled as the diameter increases, i.e. the cross-sectional area decreases and thus the heat in-leak is reduced. However, the reduced cross-sectional area also implies an increase of

---

[2] The distance between the room-temperature socket and the heat-sink section does of course influence the heat in-leak at the sink, and therefore its temperature due to the limited cooling power of the cooler. Consequently, it has an impact on the heat-load at 4.5 K. This effect is not taken into account here.

the experienced stress following fluid-cold mass attraction. For SS304 this limits the minimal heat load to 0.7 W, since for smaller cross-sectional areas the tensile stress becomes unacceptable.

G11 is in the buckling-limited region for all plotted diameters. As a safety margin, half the room temperature yield stress is the maximum. This yield stress is 240 MPa for SS304 and 375 MPa for G11 [18].

Even with four G11 solid rods, the total heat in-leak is only 0.19 W. Thus G11 is chosen as the material for the warm-cold pillars. Very thin-walled tubes theoretically allow for a low heat load; however, any imperfections in wall thickness or tube wall imperfections will then have a large effect on the buckling strength.

The calculations in the preceding section are based on vertical pillars with a cross-sectional profile that is optimized for the buckling resistance versus the heat in-leak via conduction. However, it was estimated that the thermal budget, as discussed in [15], allows for vertical pillars with a larger cross-sectional area. So the chosen pillars have inner and outer diameters of 20 mm and 26.2 mm, respectively. The main motivation behind this choice is that a mechanical failure has much worse effects than a slightly higher operating temperature. If a pillar breaks, the magnet stops being useful, whereas at a slightly higher operating temperature one can still utilize the magnet with a smaller temperature margin or with a lower magnetic field. The selected pillars have a buckling strength of 10 kN, while the gravitational load is 1.3 kN. Thus a safety factor of 8 is present.

The four vertical warm-cold pillars of the demonstrator magnet introduce a heat load at 4.5 K of 138 mW, still five times lower than what can be achieved with stainless steel pillars.

It was decided that further methods to increase the buckling resistance were not necessary, since with the chosen pillar structure the heat load is low enough. For example, buckling strength can also be substantially improved by reducing the effective length L of the pillars by interconnecting them at 1 or 2 temperature levels.

The horizontal tie rods, shown in figure 17, do not experience a strong compressive load and are not in risk of buckling. The heat in-leak of four of these rods, thermalized to 77 K at half a meter from the cold mass, and with a 20 mm diameter, is estimated at 39 mW. This diameter is chosen to provide sufficient stiffness. Both the rods and tubes are manufactured by Von Roll, and the specific type of G11 is Vetronite [38]. The stresses in the pillars structure in various load-cases are the focus of the next section.

5.4. Vertical & horizontal pillar structures

Two methods are used to estimate the stress in the pillars and the rods. The first is analytical and based on the assumption that the vertical pillars handle all forces in the z'-direction and the tie rods all x'-forces:

$$F_{\text{vert-pillars}} = F_z \cos\alpha + F_{\text{mag},z'} \pm F_{\text{torque}}; \tag{12}$$

$$F_{\text{hor-pillars}} = F_z \sin\alpha + F_{\text{mag},x'}. \tag{13}$$

Table 4. Average vertical stress $\overline{\sigma}_{z'}$ in vertical warm-cold pillars and average horizontal stress $\overline{\sigma}_{x'}$ in horizontal warm-cold pillars for various load cases, calculated both using analytical expressions and a simplified 3D COMSOL model, respectively. FEM results are presented in brackets.

	Stress $\overline{\sigma}_{z'}$ (MPa)		Stress $\overline{\sigma}_{x'}$ (MPa)	
Case	Vert I	Vert II	Hor I	Hor II
Room temperature	$-6(-5)$	$-6(-6)$	$-9(-9)$	$-11(-11)$
Cool-down	$-6(-4)$	$-6(-5)$	$-1(0)$	$-3(-2)$
High torque	$-5(-4)$	$+17(+17)$	$+4(+2)$	$-7(-5)$
Full fluid bed	$+19(+19)$	$+24(+24)$	$0(-2)$	$-5(-5)$

The torque on the tilted cassette due to the force between coils and ferrofluid only causes stress in the vertical pillars, as the tie rods are assumed to be parallel to the cassette.

When the cold mass is cooled down to 4.5 K the vertical pillars shrink and the cold mass is free to move down due to the low stiffness of the tie rods in their transverse direction. Thus no thermal stress is created in the bulk of the vertical pillars. The connection of the pillars to the fixture on the cold side was evaluated in section 4.4. The tie rods do develop a thermal stress and this will be estimated next.

The cassette itself is considered to be a rigid object that shrinks by 0.37%. This corresponds to the shrinkage of the cold mass in the x'-direction as calculated in section 4.4. The assumption of a rigid object can be made since the pillars have a low stiffness compared to the cassette.

The tie rods are thermalized roughly half a meter from the cassette and have a total length of 0.72 m. The fibre direction is longitudinal. To estimate the thermal contraction of these tie rods, a simple 1D FEM calculation is performed in which the tie rod is divided into a section of 0.22 m with one end at 293 K and the other end at 77 K, and a 0.5 m section with one end at 77 K and the other at 4.5 K. Thermal contraction and conductivity are taken from [18]. The result is that the tie rod shrinks 0.194%.

Part of the contraction will not result in stress, as the cold end of the tie rod is allowed to move over a distance $\Delta x' = -1.1\ mm$ due to the shrinking cassette. The resulting thermal stress on the tie rods is 8 MPa.

The stress in the pillars during different loading scenarios are presented in table 4. The two analysed scenarios are those in which the total force and in which the exerted torque are maximum. The first scenario corresponds to normal operation in which the magnet is fully energized and attracts the entire fluid volume, the second one to a situation where part of the fluid is accidentally obtained and a highly asymmetric force balance occurs. Data from a COMSOL model agree well with analytical estimates. During all load-cases the stress is well below the allowed values. The vertical pillars are under compression unless the magnet is energized and there is a ferrofluid present, see figure 1. At this point, it depends on the filling level of the fluid tank whether the Vert I pillars see a compressive- or a tensile force.

The mentioned simulation model has a geometry, see figure 21, representing the coils and pillars, as well as a 1-piece

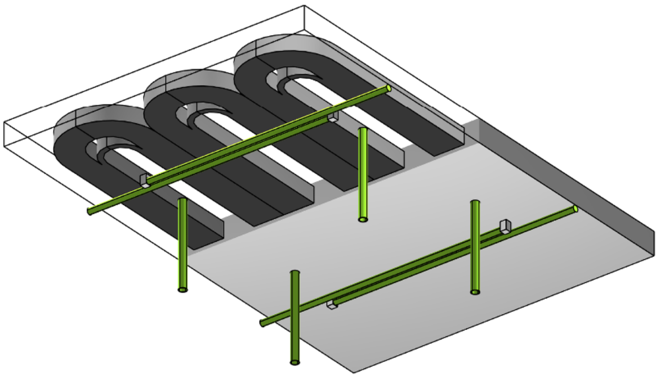

Figure 21. Simplified geometry used in simulation of the pillar-cold mass structure. The mechanical cassette is modelled as a single object with mixed properties of the aluminium alloy, stainless steel yoke, and copper pieces making up the actual cassette. Half of this object is shown in the figure.

cassette-yoke-copper composite. The total mass of the combined object is 520 kg.

When comparing the vertical displacement of the cold mass after cool-down (−0.5 mm) and upon energizing, it is found that the coils move up by 0.37 mm due to the ferrofluid-magnet attraction, in the case of a full fluid bed.

6. Conclusion

The paper dealt with the mechanical design of a conduction-cooled NbTi-based MDS demonstrator magnet. The cryostat of the system has a main vessel housing the cold mass and a turret in which a cryocooler and other services are placed. The novelty of the cryostat is that it has a large flat surface facing the ferrofluid, in order to minimize the distance between ferrofluid and coils. This 50.5 mm distance between the cryostat and the top surface of the coil is made up from components listed in table 1.

The top plate of the cryostat is supported by room-temperature stainless steel columns passing through holes in the cold mass. They allow the top plate to be relatively thin (20 mm). This column structure is advantageous for more powerful MDS magnets as well, despite the added complexity in cold mass construction and cryostat. By opting for conduction-cooling of the cold mass, a double-walled cryostat is not necessary. The performance of the demonstrator is a factor 2 higher than that of a bath-cooled system that does not use the column structure.

Several concepts for cold mass design were presented. The selected design uses a cassette consisting of two aluminium-alloy machined plates that shrink-fit around the coils during cool-down and provide a compressive force on the winding pack. Underneath the cassette, high-purity aluminium heat drains ensure that the thermal gradient across the cold mass is smaller than 100 mK. It was found that the bolts that connect the two cassette halves gain a significant tensile stress of up to 140 MPa during cool-down, due to differential thermal shrinkage.

The main factor determining the minimum cassette thickness, 12 mm per plate for the demonstrator, is the amount of pre-compression required to prevent positive transverse stress in the winding pack due to the Lorentz force. The effects of the thickness on the longitudinal stress in the winding pack and on the von Mises stress in the cassette itself are shown to be secondary importance.

The cold mass is kept in place using a fibreglass pillar and tie rod structure, the dimensions of these were optimized to minimize heat in-leak. The support structure can handle both compressive and tensile loads, without yielding or buckling. G11 is found to be the optimum material choice to withstand buckling with a minimum heat in-leak.

Data availability statement

No new data were created or analysed in this study.

Acknowledgments

This research is part of the programme Innovative Magnetic Density Separation (IMDS), which is supported by NWO, the Netherlands Organization for Scientific Research, domain Applied and Engineering Sciences and partly funded by the Dutch Ministry of Economic Affairs.

ORCID iDs

J J Kosse https://orcid.org/0000-0003-2382-8495
C Zhou https://orcid.org/0000-0001-7895-0872
G Tomás https://orcid.org/0000-0002-3197-8330
H H J ten Kate https://orcid.org/0000-0001-5597-3190

References

[1] Hu B 2014 Magnetic Density Separation of polyolefin wastes *PhD Dissertation* University of Delft, Delft

[2] Bakker E, Rem P C and Fraunholcz N 2009 Upgrading mixed polyolefin waste with magnetic density separation *Waste Manage.* **29** 1712–17

[3] Serranti S, Luciani V, Bonifazi G, Hu B and Rem P C 2005 An innovative recycling process to obtain pure polyethylene and polypropylene from household waste *Waste Manage.* **35** 15–20

[4] Muchova L, Bakker E and Rem P C 2009 Precious metals in municipal solid waste incineration bottom ash *Water Air Soil Pollut: Focus* **9** 107

[5] Bakker E, Berkhout A, Hartmann L and Rem P C 2010 Turning magnetic density separation into green business Using the cyclic innovation model *Open Waste Manage. J.* **3** 99-116

[6] Luciani V, Bonifazi G, Rem P C and Serranti S 2015 Upgrading of PVC rich wastes by magnetic density separation and hyperspectral imaging quality control *Waste Manage.* **45** 118–25

[7] van Silfhout A M, Engelkamp H and Erné B H 2020 Colloidal stability of aqueous ferrofluids at 10 T *J. Phys. Chem. Lett.* **11** 5908–12

[8] Svoboda J 2004 *Magnetic Techniques for the Treatment of Materials* (Dordrecht: Kluwer)

[9] Smolkin R D, Krohmal V S and Sayko O P 1993 Commercial Equipment Designed to Recover Gold From Gravitational Concentrates by Means of Magnetic Separation and Separation in Magnetic Fluids *Proc. Xviii Int. Mineral Processing Congress* (Sydney: The Australasian Institute of Mining and Metallurgy, Melbourne) pp 425–31

[10] Svoboda J 2000 Separation in magnetic fluids: time to meet the technological needs *Proc. MINPREX 2000th Conf.* (Melbourne: The Australasian Institute of Mining and Metallurgy, Carlton) 297–301

[11] Svoboda J 2004 Densimetric separation of coal using magnetic fluids *Phys. Sep. Sci. Eng.* **13** 127–39

[12] Kosse J J, Dhallé, M, Rem P C, ter Brake H J M and ten Kate H H J 2021 Fundamental electromagnetic configuration for generating one-directional magnetic field gradients *IEEE Trans. Magn.* **57** 8001810

[13] Kosse J J, Dhallé M, Tomás G, ter Brake H J M and ten Kate H H J 2022 Performance estimates of superconducting magnetic density separation Manuscript in preparation

[14] Kosse J J, Dhallé M, Tomás G, Rem P C, ter Brake H J M and ten Kate H H J 2021 Optimum coil-system layout for magnet-driven superconducting magnetic density separation *IEEE Trans. Magn.* **57** 9000209

[15] Kosse J J, Wessel W A J, Zhou C, Dhallé M, Tomás G, Krooshoop H J G, ter Brake H J M and ten Kate H H J 2021 Thermal and electrical design of a superconducting magnetic density separation demonstrator (in preparation)

[16] Brown G, Halbach K, Harris J and Winick H 2022 Wiggler and undulator magnets—a review *Nucl. Instrum. Methods Phys. Res.* **208** 65–77

[17] Jaeschke E J *et al* 2019 *Synchrotron Light Sources and Free-Electron Lasers* (Switzerland AG: Springer Nature)

[18] Ekin J W 2006 *Experimental Techniques for Low Temperature Measurements* (Oxford: Oxford University Press)

[19] Thermal Insulation Products—COOLCAT 2 NW 2019 RUAG Space

[20] Kostrov E, Bagdinov A and Demikhov E *et al* 2015 Performance test of a G-M cooler in magnetic field *Phys. Procedia* **67** 440–4

[21] Timoshenko S P 1955 *Strength of Materials pt. 1, Elementary Theory and Problems* (Lancaster, Pennsylvania: Lancaster Press, Inc.)

[22] İmrak C E and Gerdemeli İ 2007 An Exact Solution for the Deflection of a Clamped Rectangular Plate under Uniform Load *Appl. Math. Sci.* **1** 2129–37

[23] Iwasa Y 2009 *Case Studies in Superconducting Magnets* (Berlin: Springer)

[24] Wilson M N 1987 *Superconducting Magnets* (Oxford: Clarendon)

[25] Ekin J W, Schramm R E and Clark A F 1978 *Effect of Strain on Epoxy-Impregnated Superconducting Composites, a Chapter in Nonmetallic Materials and Composites at low Temperatures* (New York: Plenum Press)

[26] Hagedorn J, Sell-Le Blanc F and J 2017 *Handbook of Coil Winding: Technologies for Efficient Electrical Wound Products and Their Automated Production* (Berlin: Springer Vieweg)

[27] Foner S and Schwartz B B 2012 *Superconductor Materials Science: Metallurgy, Fabrication and Applications* (Singapore: Springer Science & Business Media)

[28] Gray W H and Sun C T 1976 *Theoretical and Experimental Determination of Mechanical Properties of Superconducting Wire* (Oak Ridge, Tennessee: Oak Ridge National Laboratory)

[29] Clark A F *et al* 1976 *Characterization of a Superconducting Coil Composite and its Components* (National Bureau of Standards)

[30] Ledbetter H M and Read D T 1977 Orthorhombic constants of an NbTi/Cu composite superconductor *J. Appl. Phys.* **48** 141–6

[31] Hicks C W *et al* 2014 Strong increase of T_c of Sr_2RuO_4 under both tensile and compressive strain *Science* **344** 283–5

[32] Barth C *et al* 2013 Degradation free epoxy impregnation of REBCO coils and cables *Supercond. Sci. Technol.* **26** 055007

[33] Rossi L 2003 Superconducting Magnets for the LHC Main Lattice *Conf.: Magnet Technology 18*

[34] van Silfhout A and Erné B 2019 Magnetic detection of nanoparticle sedimentation in magnetized ferrofluids *J. Magn. Magn. Mater.* **472** 53–8

[35] Kaufman J G 1999 *Properties of Aluminum Alloys: Tensile, Creep and Fatigue Data at High and Low Temperatures* (Materials Park, Ohio: The Aluminum Association)

[36] Kaufman J G 2011 *Relational Analysis: Guidelines for Estimating High and Low Temperature Properties of Metals* (Materials Park, Ohio: ASM International)

[37] van de Camp W *et al* 2015 Cryogenic fatigue and stress-strain behavior of a fibre metal laminate *Phys. Proc.* **67** 1043–8

[38] Runde Rohre Vetronit Cryo T 2018 Von Roll Deutschland GmbH, datasheet WHA C07TVGC612 27–8

[39] Huber J E, Nowell D and Hills D A 2007 On the stress analysis of a wound coil with application to electromagnet manufacture *J. Strain. Anal. Eng. Des.* **42** 447–60